Compositional study of a corrosion protective layer formed by leachable lithium salts in a coating defect on AA2024-T3 aluminium alloys

Marcoen, Kristof; Visser, P.; Trindade, G. F.; Abel, M. L.; Watts, J. F.; Mol, J. M.C.; Terryn, H.; Hauffman, T.

DOI
10.1016/j.porgcoat.2018.02.011

Publication date
2018

Document Version
Final published version

Published in
Progress in Organic Coatings

Progress in Organic Coatings 119 (2018) 65–75

Contents lists available at ScienceDirect

Progress in Organic Coatings

journal homepage: www.elsevier.com/locate/porgcoat

Compositional study of a corrosion protective layer formed by leachable lithium salts in a coating defect on AA2024-T3 aluminium alloys

K. Marcoen[a,*], P. Visser[b,c], G.F. Trindade[d], M.-L. Abel[d], J.F. Watts[d], J.M.C. Mol[b], H. Terryn[a,b], T. Hauffman[a]

[a] Vrije Universiteit Brussel, Research Group of Electrochemical and Surface Engineering (SURF), Pleinlaan 2, 1050 Brussels, Belgium
[b] Delft University of Technology, Department of Materials Science and Engineering, Mekelweg 2, 2628 CD Delft, The Netherlands
[c] AkzoNobel, Specialty Coatings, Rijksstraatweg 31, 2171 AJ Sassenheim, The Netherlands
[d] The Surface Analysis Laboratory, Department of Mechanical Engineering Sciences, University of Surrey, Guildford, Surrey GU2 7XH, United Kingdom

ARTICLE INFO

Keywords:
Corrosion
Inhibition
Leaching
Aluminium
Lithium
Coating
ToF-SIMS
Multivariate analysis
NMF

ABSTRACT

Organic primer coatings loaded with environmentally harmful Cr(VI) corrosion inhibitive pigments still play an important role in corrosion protection of aluminium alloys for the aerospace industry. A potential "green" alternative coating system has recently been developed, loaded with lithium salt corrosion inhibitors. Under exposure to neutral salt spray, lithium salts leach from the organic coating into coating defects to induce the formation of a corrosion protective layer. In this work the composition and growth of this protective layer is investigated by time-of-flight secondary ion mass spectrometry (ToF-SIMS). ToF-SIMS imaging is successfully applied to monitor the lateral spread of leaching lithium salts in artificial 1-mm-wide scribes. The chemical composition of the protective layer is revealed by comparing the mass spectra of salt spray exposed scribe areas to the mass spectra of pseudoboehmite and aluminium-lithium layered double hydroxide reference samples. The insights obtained in this work have led to a thorough understanding of the formation mechanism of the protective layer and provide local chemical and structural information which can be linked to corrosion protection behavior.

1. Introduction

Aluminium alloys such as AA2024-T3 are widely used in the aerospace industry because of their remarkably high strength-to-weight ratio. However, as these alloys are highly susceptible to localized corrosion, they require an advanced corrosion protection scheme. International restrictions on the use of toxic and environmentally harmful Cr(VI) corrosion inhibitors have boosted the development of alternative environmental friendly metal surface pretreatments for many years now [1].

In the 1990s, aluminium-lithium conversion coatings were proposed, as several reports described passivity of Al and Al alloys after immersion in alkaline lithium salt solutions [2,3]. At the time this was unexpected, as aluminium shows a high dissolution rate in alkaline solutions at pH values above 9. However, in alkaline lithium salt solutions, stable corrosion-resistant surface films were obtained [3,4]. X-ray diffraction (XRD) showed that the coating formed on aluminium from lithium carbonate solutions exhibited a structure that could be linked to a compound whose stoichiometry was $Li_2[Al_2(OH)_6]_2{\cdot}CO_3 \cdot nH_2O$, a lithium aluminium hydroxide carbonate hydrate which can be categorised as a layered double hydroxide (LDH) [4]. This structure has also been proposed for a coating formed on AA1100 [5]. Although these aluminium-lithium conversion coatings offered good protection against corrosion, it remains a major challenge to (fully) replace chromate based corrosion inhibition by systems that show the same level of effectiveness, especially at the aeronautical industry [6].

Recently, lithium salts have been proposed as a potential replacement for chromate-containing pigments in organic coatings [7–11]. Under exposure to neutral salt spray conditions (ASTM B-117), lithium carbonates and lithium oxalates were shown to leach out of the organic coating to form a protective layer in an artificial defect on AA2024-T3 [7,8]. The effective corrosion protective properties of these layers were demonstrated by Visser et al. in a study based on electrochemical techniques [12]. The formed layers were also investigated in terms of morphology by electron microscopic techniques; a variety of morphologies have been described [10,11]. Cross-sectional analysis showed that in general three regions can be distinguished, comprising a dense layer near the substrate, a porous layer in the middle and a columnar layer on top [7,11]. Transmission electron microscopy equipped

* Corresponding author.
E-mail address: Kristof.Marcoen@vub.be (K. Marcoen).

https://doi.org/10.1016/j.porgcoat.2018.02.011
Received 11 September 2017; Received in revised form 16 December 2017; Accepted 19 February 2018
Available online 28 February 2018
0300-9440/

with electron energy loss spectroscopy (TEM-EELS) revealed that the entire coating was mainly composed of aluminium, lithium and oxygen [7,11]. Despite varying morphologies in different regions of the scribed area, the layer overall offered good protection against corrosion [10,11]. Different morphologies may be a consequence of differences in the local concentration of lithium [10,11], which suggests that more than one composition is present within the protective layer. An X-ray photoelectron spectroscopy (XPS) analysis indicated the presence of a hydrated aluminium oxide in the form of a pseudoboehmite with lithium incorporated in its matrix [8], but did not explain the presence of different morphologies. A compositional analysis of the protective layer by XPS is in the first place limited by a low sensitivity towards lithium. In addition, due to its low lateral resolution, XPS may not be able to distinguish the different phases that seem to coexist in the scribe.

In this work, the protective layer formed on AA2024-T3 by leaching lithium carbonates is investigated using time-of-flight secondary ion mass spectrometry (ToF-SIMS), with the aim to specify the layer's composition(s). The choice for ToF-SIMS is mainly governed by its large sensitivity towards lithium compared to XPS, energy-dispersive X-ray spectroscopy (EDX) and Auger electron spectroscopy (AES). Its large potential for the speciation of inorganic compounds has been demonstrated on a variety of materials [13,14]. Given the high lateral resolution that can be achieved, ToF-SIMS imaging has been applied to monitor the lateral growth of a lithium based protective layer within artificial 1-mm-wide scribes exposed to a neutral salt spray. Characteristic ion fragment assignments were made for hydrated aluminium oxide (pseudoboehmite (PB)) and lithium-aluminium layered double hydroxide (LDH) reference samples, and subsequently used to differentiate growth regions in terms of chemical composition. Multivariate analysis methods (i.e., principal components analysis (PCA) and non-negative matrix factorisation (NMF)) are applied to transform the complex ToF-SIMS dataset to a scale that defines whether the surface coverage in a sample region is composed of PB or LDH.

2. Materials and methods

Analytical grade purity lithium carbonate, provided by Sigma–Aldrich, was used as corrosion inhibitive pigment and formulated into an organic model coating. A polyurethane binder chemistry was selected since it is inert to the other ingredients and demonstrated leaching of the lithium inhibitor [6]. The coating was formulated as a white opaque primer using pigments and extenders in addition to the corrosion inhibitor. The pigment volume concentration of lithium carbonate was 15% (V/V). Organic and inorganic compounds used in the coating are listed in Table 1, as well as their amounts. Coatings were prepared as described by Liu et al. [11]. AA2024-T3 substrates of 0.8 mm thickness were provided by Alcoa (AA2024-T3QQ-A250/5) and were tartaric sulphuric acid (TSA) anodized according to aerospace requirements (AIPI 02-01-003) at Premium AEROTEC, Bremen, Germany. Coatings were applied with a high volume low pressure (HVLP) spray gun. After curing at 80 °C for 16 h and a 1-h flash-off at 23 °C, coating thicknesses were between 20 and 25 µm.

Coated panels, with dimensions of 7 cm × 7 cm were artificially damaged with a carbide steel milling blade. 1-mm-wide scribes were made from corner to corner (St. Andrews cross), penetrating to a depth of 100–150 µm into the metal. The samples were covered with tape on the backside and sides, and exposed to a 5% (w/w) NaCl neutral salt spray (NSS) according to ASTM-B117 for varying periods of time (15 min, 1 h and 48 h) to study formation of the protective layer and the composition of the different morphologies observed during the very early stages of formation and after prolonged exposure [11]. After exposure, the process was quenched by rinsing the samples for 2 min with flowing deionized water (to remove residual chlorides) and subsequent air drying.

Table 1
Composition of the model organic coatings [7,11].

	Supplier	Amount (g)
Component A		
N-Butylacetate	Sigma–Aldrich	75.0
Desmophen 650 MPA	Bayer materials science	47.7
Lithium carbonate	Sigma–Aldrich	23.6
Magnesium oxide	Sigma–Aldrich	16.4
TiOxide TR 92	Huntsman	5.9
Component B		
Tolonate HDB 75 MX	Vencorex	28.5
Dynasilan Glymo	Evonik	5.2

Reference compositions were prepared on AA2024-T3 bare substrates. Prior to treatment, all aluminium alloy panels were cleaned with acetone (> 99.9%, SASOL Chemie Gmbh & Co. KG) and scribed as the coated panels. Pseudoboehmite (PB) references were prepared by immersion of the panels (i) in deionized water (DIW) or (ii) in a 0.02 M LiCl solution (BioXtra, ≥99.0%, Sigma–Aldrich) in DIW, at 95–100 °C for 1 h according to the method of Gorman et al. [15]. Hereafter, the reference prepared in a LiCl solution will be denominated as L-PB, to make a distinction with the PB reference prepared in DIW. An aluminium-lithium layered double hydroxide (LDH) conversion coating was prepared using the conversion coating process as described by Buchheit et al., by immersing a AA2024-T3 panel in a 0.1 M lithium carbonate solution in DIW (pH 11.3) for 15 min [4]. After the treatments, all panels were rinsed with DIW for 5 min and dried at the air. Measurements were performed in the scribed areas.

2.1. Time-of-flight secondary ion mass spectrometry

ToF-SIMS measurements were performed with a TOF.SIMS 5 system from ION-TOF GmbH (Münster, Germany), using a 30 keV Bi_3^+ primary ion beam operated in the high current bunched mode for high mass resolution (approximately 8000 at 29 µm ($^{29}Si^+$)). The lateral resolution achieved in high current bunched mode is 3 µm. The pulsed ion beam target current was approximately 0.37 pA. Positive ion mass spectra were acquired over a mass range of 1–800 µm and calibrated using a list of fragments of known composition, such as CH_3^+, $C_2H_3O^+$, $LiOH^+$, $AlOH^+$ and Al_2^+. The accuracy of a mass assignment (in ppm) is calculated by taking the absolute difference between the experimental and theoretical mass of a fragment and dividing this number by the experimental mass.

Mass spectra of reference samples were obtained by rastering areas of 100 µm × 100 µm, at 128 × 128 pixels. The analysis time was 60 s, keeping the total ion dose below the static limit of 1×10^{13} ions cm^{-2} $analysis^{-1}$. Large area images were obtained in the scribes of NSS exposed samples by rastering an area of 800 µm × 2000 µm, divided into 10 patches of 400 µm × 400 µm. Each patch was analysed for 60 s, with a pixel density of 250 pixels/mm. A high spectral resolution peak list was first created for the reference samples by identification of characteristic ion fragments and subsequently applied to spectra obtained by large area imaging of NSS exposed scribes.

2.2. Multivariate analysis methods

Large area imaging provided a large amount of data, as each pixel in a ToF-SIMS image contains a complete mass spectrum. Multivariate analysis (MVA) methods were used as a tool for efficient data analysis. Principal component analysis (PCA) was applied in order to check for the source of variability in the data. Variables in a SIMS dataset are the intensities of mass peaks obtained for different observations. PCA reduces this dataset by constructing principal components (PCs) as new variables. PCs are characterised by loadings (positive and negative contributions of different mass peaks (old variables)) and provide a score for every sample or sample region. Scores point out whether different spectra or observations are related to each other, while the corresponding loadings explain how they are related [16,17]. PCs are

ordered by captured variance within the original dataset. Often only a few PCs have to be considered to explain more than 95% of the total variance. In a ToF-SIMS dataset, variance is largely attributed to different sample compositions or sample matrix effects.

Given that the loadings in PCA are defined by positive and negative contributions of mass peaks, its outcome cannot be directly related to mass spectra. Non-negative matrix factorisation (NMF) is an MVA method that does provide results that can be directly linked to mass spectra and distribution maps. This makes NMF output easier to interpret and visualise, especially in the field of surface chemistry [18]. NMF starts from a matrix **A** containing mass fragments in its rows and observations in its columns. Using a multiplicative algorithm created by Lee and Seung [19], matrix **A** can be approximately factorised (**A** ≈ **HW**) into non-negative matrices **H** and **W**. **H** represents the characteristic spectra of a defined number of 'pure compounds' present in the samples and **W** represents the 'concentrations' of these compounds in each observation. The number of compounds is a constraint that should be given at the start of an NMF analysis [18]. In this work, PCA was used as an exploratory tool to estimate the number of chemical compounds present in the samples. This number was then used as a constraint for NMF factorisation of the original ToF-SIMS dataset (100 iterations).

Each MVA analysis was performed on Matlab R2015a (Mathworks), using the simsMVA app developed by Trindade et al. [18,20,21]. Preprocessing steps for PCA analysis include normalisation by total ion counts, Poisson scaling and mean centering of all data. Preprocessing steps for NMF analysis include normalisation by total ion counts and Poisson scaling.

3. Results

3.1. Lithium leaching

The influence of neutral salt spray (NSS) exposure on a scribed area was evaluated by mass spectrometry. Fig. 1 shows the positive mass spectrum (0–50 *m/z*) of a scribed panel NSS exposed for 15 min compared to the spectrum of an unexposed blank. The main difference observed in this mass range is two peaks at nominal masses 6 and 7 (*m/z*), appearing in the NSS exposed sample only. These peaks can be assigned to the positive lithium ion Li^+ and its minor isotope $^6Li^+$ and thus show the presence of lithium in the scribe after NSS exposure. The significantly higher intensity for Na^+ (m/z = 23) in the exposed panel can be explained by the neutral salt spray exposure. The hydrocarbons observed in both spectra are attributed to surface contamination. It is also noteworthy, for the NSS exposed spectrum, that Li^+ and Al^+ signals were both saturated. This means that the reported Li^+ and Al^+ counts are underestimations for the real amount of ions that have reached the detector.

Fragments of interest, Li^+, $^6Li^+$ and $AlOH^+$, are selected from the mass spectra and mapped for a large area (800 µm × 2000 µm). Fig. 2 shows ToF-SIMS images of scribes that were NSS exposed for 15 min and 1 h. Due to detector saturation, Li^+ and Al^+ (as a substrate peak) are not suitable to monitor the leaching of lithium salts in the scratch. However, from the saturated Li^+ images (Fig. 2a and d), it can be concluded that the spread of lithium in the scribe goes relatively fast; after 15 min NSS exposure, the 1-mm-wide scribe was already completely covered with lithium. Unlike Li^+, the $^6Li^+$ isotope peak is not saturating the detector, as ^6Li only has a natural abundance of 7.59%. This makes $^6Li^+$ most suitable to map the distribution of lithium within the scribe. Large regions with significantly varying lithium concentrations are distinguishable in the $^6Li^+$ images (Fig. 2b and e). By comparing the $^6Li^+$ images to the $AlOH^+$ images (Fig. 2c and f) it can be assumed that lower concentrations of lithium coincide with higher concentrations of aluminium. Based on the concentration differences and based on the different morphologies that are known to be present in the scribe [8,11], it can be expected that the surface coverage of these scribes is made up of different compositions.

3.2. Compositional study by comparison with reference samples

The composition of the protective layer is investigated through an indirect speciation analysis, i.e. specific secondary ions and their intensity ratios in the mass spectra of reference samples are applied as fingerprints to identify inorganic compounds. Based on intensity variations in the $^6Li^+$ images of 15 min and 1 h NSS exposed scribes, regions of interest (ROIs) were selected (Fig. 3). Mass spectra obtained from ROIs with lower $^6Li^+$ intensities (ROI 1 and 4) and mass spectra obtained from ROIs with higher $^6Li^+$ intensities (ROI 2, 3 and 5) are compared to the mass spectra of reference samples. Reference spectra and the mass spectra obtained from ROI 4 and 5 are presented in Fig. 4 (mass range 0–100 *m/z*) and Fig. 5 (mass range 100–200 *m/z*).

Mass spectra of a reference PB prepared in DIW, a reference PB prepared in a LiCl solution (L-PB) and a reference LDH are shown in Fig. 4, labeled as a, b and d, respectively, for the 0–100 *m/z* mass range. Mass peaks attributed to $^6Li^+$ and Li^+ (at 6 and 7 *m/z*, respectively), show that lithium is incorporated in the LDH and L-PB structures, but absent for PB. Peaks at nominal masses 31, 73 and 91 *m/z* are found to be characteristic for the LDH spectrum and can be assigned to lithium-rich fragments Li_2OH^+, $Li_2AlO_2^+$ and $Li_2AlO_3H_2^+$, respectively.

The compositional differences between the PB references and LDH become even more clear in the 100–200 *m/z* mass range shown in Fig. 5, where peaks at nominal masses 103, 121, 146 and 163 *m/z*,

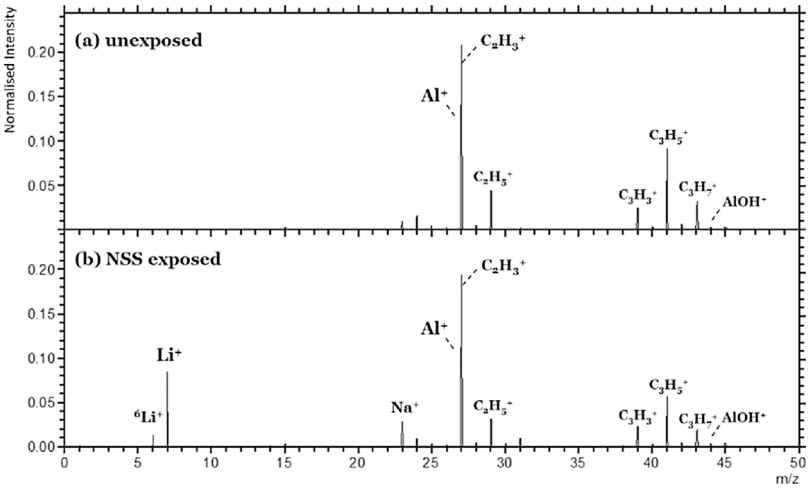

Fig. 1. Positive mass spectrum obtained in a scribe (a) unexposed and (b) NSS exposed for 15 min. Mass range 0–50 *m/z*. Mass spectra are normalised to total ion intensity.

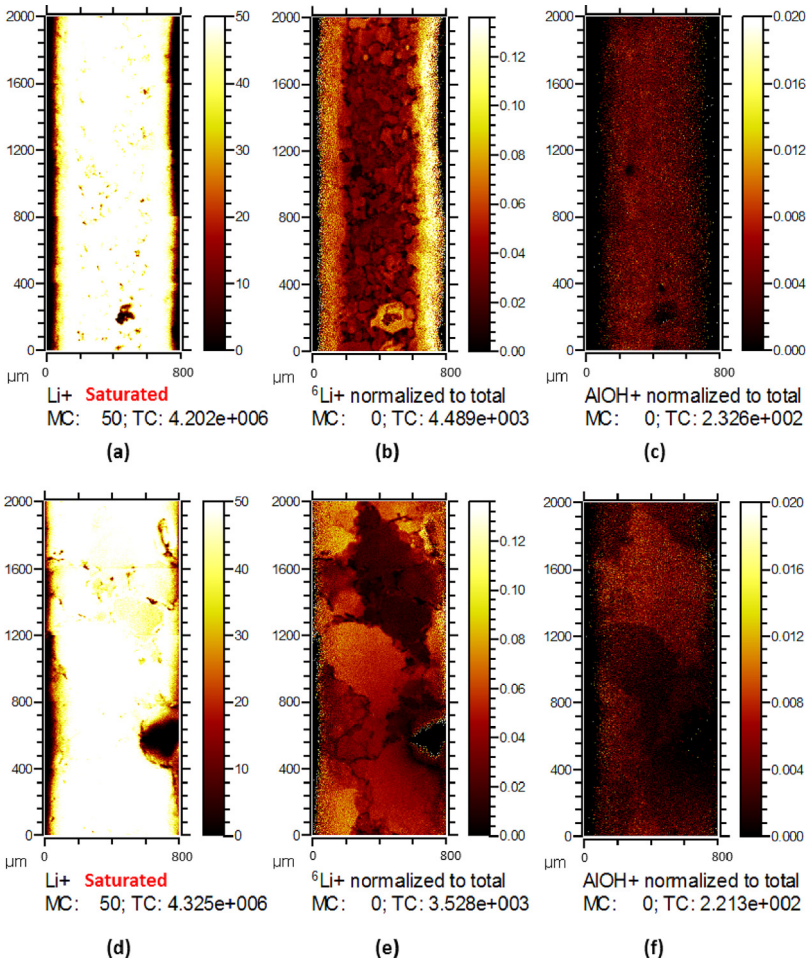

Fig. 2. Large area (800 µm × 2000 µm) ToF-SIMS images (top) of a 15 min NSS exposed scribe: (a) Li^+, (b) $^6Li^+$, (c) $AlOH^+$, (bottom) of a 1 h NSS exposed scribe, (d) Li^+, (e) $^6Li^+$, (f) $AlOH^+$. All images, except for the Li^+ images, are normalized to total ion intensity.

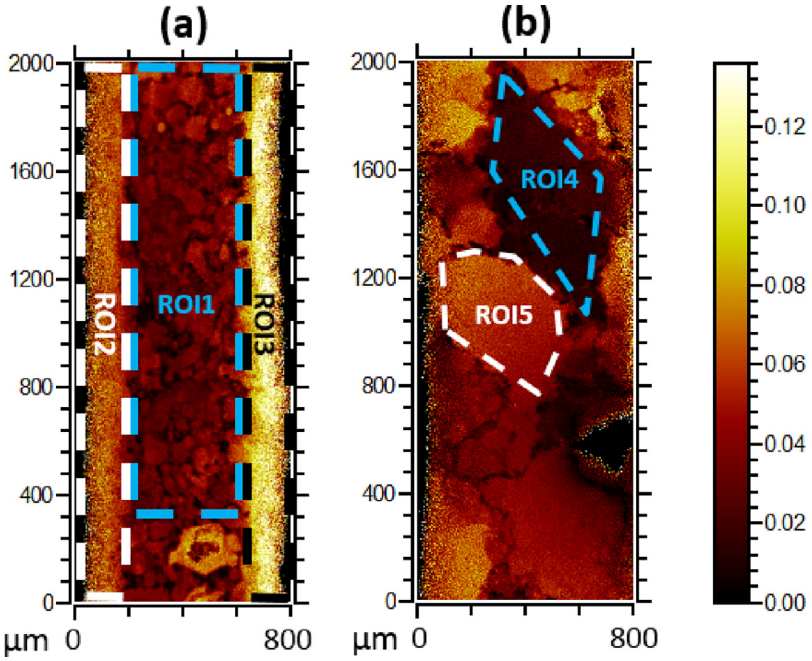

Fig. 3. Based on intensity variations in the $^6Li^+$ images, regions of interest (ROIs) are defined for (a) the 15 min NSS exposed scribe and (b) the 1 h NSS exposed scribe. All images were normalized to total ion intensity.

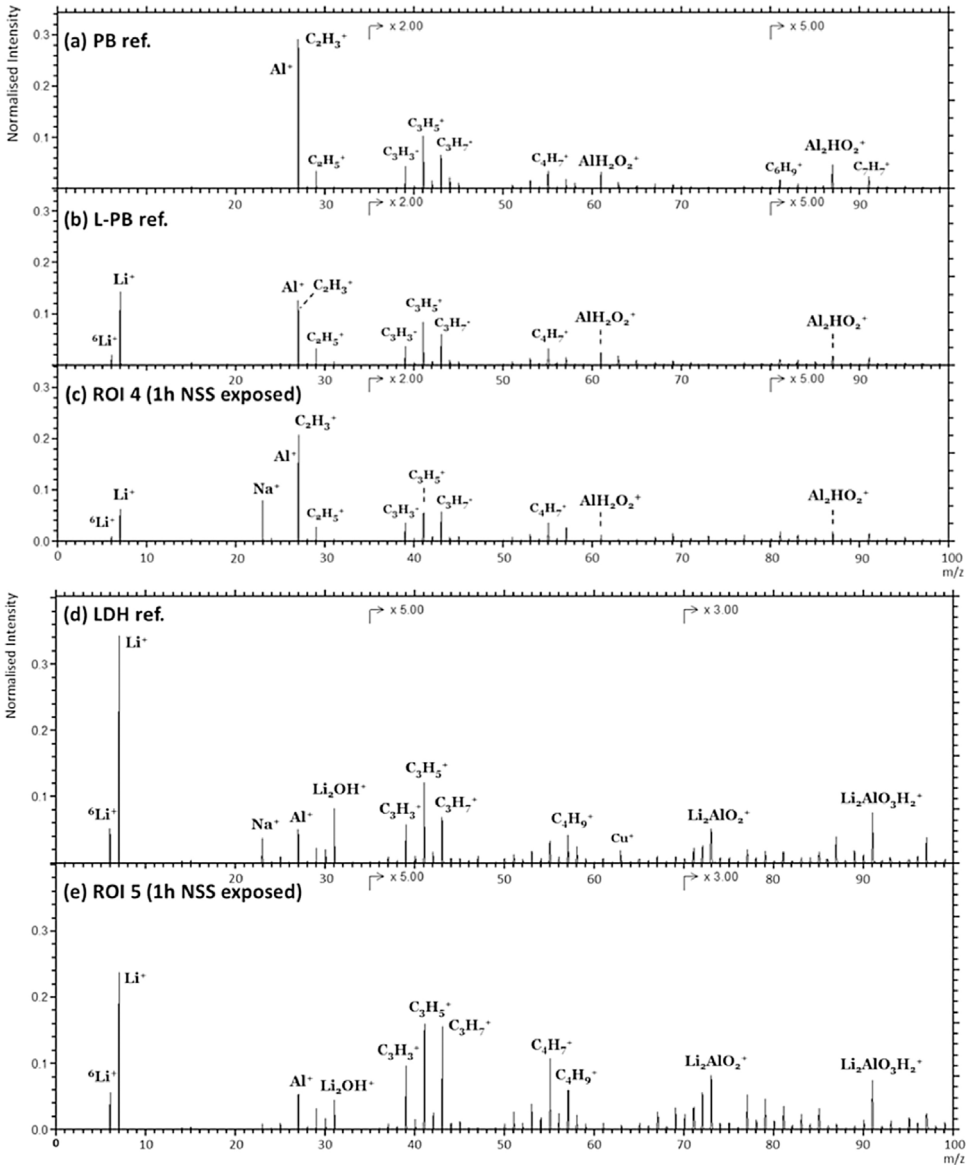

Fig. 4. Overlay of positive ToF-SIMS mass spectra in the mass range 0–100 *m/z* obtained from (a) the PB reference, (b) the L-PB reference, (c) ROI 4 from the 1 h NSS exposed scribe, (d) the LDH reference, and (e) ROI 5 from the 1 h NSS exposed scribe. All mass spectra are normalised to total ion intensity.

characteristic for PB and L-PB structures, are assigned to $Al_2HO_3^+$, $Al_2H_3O_4^+$, $Al_3HO_4^+$ and $Al_3H_2O_5^+$, respectively. The LDH spectrum, on the other hand, is dominated by lithium-rich fragments as $Li_2AlO_4H_4^+$, $Li_2Al_2O_4H^+$ and $Li_2Al_2O_5H_3^+$, which are found at nominal masses 109, 133 and 151 *m/z*, respectively.

With exception of $^6Li^+$ and Li^+, PB and L-PB mass spectra are dominated by the same mass fragments. However, opposite to the PB spectrum, $Al_2H_3O_4^+$ is more dominant than $Al_2HO_3^+$ and $Al_3H_2O_5^+$ is more dominant than $Al_3HO_4^+$ in the L-PB spectrum. This suggests that the surface hydration level is higher for L-PB and is in agreement with literature, where a higher surface hydration level was reported for a PB prepared in a NaCl solution, compared to a PB prepared in DIW [15]. Hereafter, mass peaks characteristic for L-PB as well as for PB references will be referred to as PB mass peaks. A detailed overview of all assignments of characteristic LDH and PB mass peaks is given in Table 2. Characteristic LDH peaks are coded as “LDH-x”, PB peaks are coded as “PB-x”.

Detailed spectra of the peaks are shown in the appendix (Figs. A.1–A.3). It is important to notice that all fragments reported in Table 2 can be found both for LDH as for L-PB samples, albeit with large intensity differences. A clear distinction between L-PB and LDH from mass spectra can only be made by considering the differences in ion intensity ratios.

Spectra obtained from ROIs defined in Fig. 3 were compared to the reference spectra. Figs. 4 and 5 show that the lithium-poor ROI 4 matches best with the L-PB reference, while the lithium-rich ROI 5 matches with the LDH reference. One can therefore conclude that ROI 4 is covered with a L-PB layer, while in ROI 5 the surface layer is composed of LDH. Although identification of ROIs 4 and 5 went relatively straightforward, some ROIs were more difficult to assign, as their spectra are dominated by a mixture of PB and LDH peaks. In order to make an efficient and robust assignment for all ROIs, ToF-SIMS data is further processed using multivariate analysis techniques.

3.3. Multivariate analysis

A peak list created from the assignments in Table 2 was loaded into the mass spectra obtained from ROIs in the NSS exposed scribes. PCA was performed on the resulting dataset, which contains a selection of peak intensities for each ROI. Fig. 6a shows the distribution of explained variance by principal components PC1, PC2 and PC3. Other

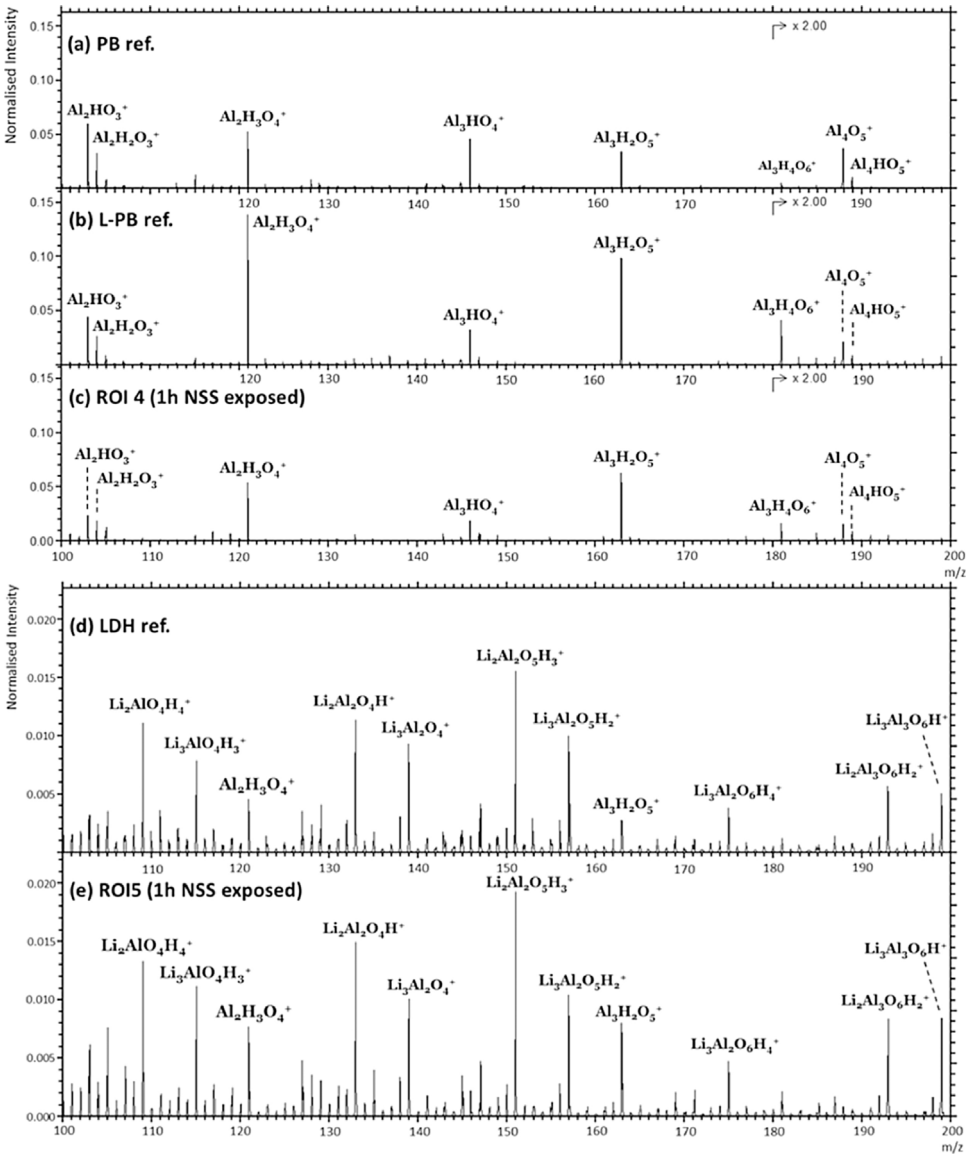

Fig. 5. Overlay of positive ToF-SIMS mass spectra in the mass range 100–200 *m/z* obtained from (a) the PB reference, (b) the L-PB reference, (c) ROI 4 from the 1 h NSS exposed scribe, (d) the LDH reference, and (e) ROI 5 from the 1 h NSS exposed scribe. All mass spectra are normalised to total ion intensity.

PCs, representative for less than 0.5% of the explained variance, were not included in this bar graph. PC1 on its own explains about 94% of the variance in the ToF-SIMS dataset. Loadings of PC1 are shown in Fig. 6b. Positive direction loadings are solely made up of mass peaks that have been assigned as LDH peaks, while negative direction loadings correspond to characteristic PB peaks. Given their low share in explained variance, it can be assumed for all PCs other than PC1 that they are attributed to noise in the spectra.

Non-negative Matrix Factorisation (NMF) was performed on the same dataset that was processed with PCA, with addition of 5 L-PB and 5 LDH reference spectra (as well as the spectra that will be discussed in Section 3.4). Since PCA showed that the variance in the ToF-SIMS dataset is almost completely attributed to the presence of two compositions (PB-type and LDH), the dataset is factorised by NMF into two components. Fig. 7 shows the characteristic spectra for two pure compounds after 100 NMF iterations. Neither of the two compounds presented exclusive peaks, but LDH peaks have a large weight in the spectrum of compound 1, while PB peaks are the main peaks characterising compound 2. Factorisation into two pure compounds enables 'relative quantification'.

Fig. 8 shows the scores or relative 'concentrations' for all ROIs and reference samples. Considering the almost pure relative concentration values for the L-PB and LDH reference samples, it is acceptable to name compound 1 'L-PB' and compound 2 'LDH'. NMF confirms for the 1 h NSS exposed sample that ROI 4 is mainly composed of L-PB, while ROI 5 is mainly composed of LDH. For the 15 min NSS exposed sample it can be deduced from the NMF scores that the lithium-rich sides (ROI 2 and 3) are covered with an LDH surface layer. After analysis of ROIs 2, 3, 4 and 5, it seems that all lithium-rich regions have been linked to LDH, while lithium-poor regions have been linked to L-PB. ROI 1, which was considered as a lithium-poor region, on first sight does not follow this trend; the surface coverage in the center region of the 15 min NSS exposed scribe seems to consist of a mixture of LDH and L-PB, with an NMF score of 65% for L-PB and 35% for LDH. However, it is important

Table 2
Fragments characteristic for an Al-Li layered double hydroxide (LDH 1–10) and pseudoboehmite (PB 1–9).

Exp. mass [m/z]	Accuracy [ppm]	Assignment	Peak code
31.0356	45	Li_2OH^+	LDH-1
73.0025	5	$Li_2AlO_2^+$	LDH-2
91.0124	11	$Li_2AlO_3H_2^+$	LDH-3
109.0224	15	$Li_2AlO_4H_4^+$	LDH-4
132.9791	22	$Li_2Al_2O_4H^+$	LDH-5
138.9866	26	$Li_3Al_2O_4^+$	LDH-6
150.9889	24	$Li_2Al_2O_5H_3^+$	LDH-7
156.9965	27	$Li_3Al_2O_5H_2^+$	LDH-8
175.0056	33	$Li_3Al_2O_6H_4^+$	LDH-9
192.9548	33	$Li_2Al_3O_6H_2^+$	LDH-10
60.9868	6	$AlH_2O_2^+$	PB-1
102.9537	14	$Al_2HO_3^+$	PB-2
103.9619	10	$Al_2H_2O_3^+$	PB-3
120.9637	16	$Al_2H_3O_4^+$	PB-4
145.9248	47	$Al_3HO_4^+$	PB-5
162.9302	23	$Al_3H_2O_5^+$	PB-6
180.9398	28	$Al_3H_4O_6^+$	PB-7
187.8934	36	$Al_4O_5^+$	PB-8
188.9037	23	$Al_4HO_5^+$	PB-9

to note that ROIs were selected visually from intensity differences in the $^6Li^+$ maps in Fig. 3. Given the high $^6Li^+$ intensities at the sides of the 15 min NSS exposed scribe, significant variations in $^6Li^+$ intensities in the large center region, which might be present as well, are visually less pronounced in Fig. 3. This shows that one has to be cautious with the designation of 'lithium-rich' and 'lithium poor' regions.

3.4. Compositional study of a 48 h NSS exposed scribe

This section will discuss the composition of a scribe that has been NSS exposed for 48 h, by comparison to the early (15 min and 1 h) exposed scribes. A $^6Li^+$ ToF-SIMS image of the 48 h exposed scribe is shown in Fig. 9a and shows that the $^6Li^+$ intensity is much more uniformly distributed than for the early exposed scribes (Fig. 3). Three large areas of 800 µm × 2000 µm were analysed by ToF-SIMS imaging for each (15 min, 1 h and 48 h exposed) scribe under investigation. The 9 resulting mass spectra have been included to the NMF analysis performed in Section 3.3. Average NMF scores for the 15 min, 1 h and 48 h exposed scribes are shown in Fig. 9b and indicate that the fraction of LDH in the surface coverage significantly increases after a long exposure to the neutral salt spray. According to an NMF analysis which presumes that only 2 compounds are present, the relative surface coverage in the 48 h NSS exposed scribe is composed of LDH for 81%. This value approaches the average LDH score of 93% obtained for LDH reference samples (Fig. 8). One can state that the scribe is almost completely covered with LDH.

4. Discussion

4.1. Link between composition and morphology

Two compositions are identified within the lithium-based protective layer, while different types of morphology have been reported in literature. The protective layer is known to exist of three distinct regions in terms of morphology, comprising a dense barrier layer near the alloy substrate, a porous middle layer and a columnar layer on top [7,8,11]. Liu et al. reported that the relative thickness of these three layers varies from region to region. The high concentration of lithium salts and high pH at the sides of the scribe seem to induce a columnar layer with a thin underlying barrier and/or porous layer [11]. In the center of the scribe, where the concentration of lithium salts is supposedly lower due to an increased pathway for leaching, mainly barrier-type morphology was observed. With increasing exposure time to a neutral salt spray, the protective layer in the center of the scribe seems to evolve in three gradations (A-B-C) as shown in Fig. 10, going from a thick barrier layer (type A) to a barrier layer with porous surface layer (type B), to the typical three-layer morphology (type C) [11].

The compositional analysis performed in this work with ToF-SIMS is in accord with these morphological investigations. In the 15 min NSS exposed scribe, two compositions were present at the surface; the lithium-rich side regions were identified as Al-Li layered double hydroxides, while the surface layer in the center region is mainly composed of lithium-containing pseudoboehmite. Although the lithium-based protective layer was already well-characterised in terms of corrosion–protection behaviour [12] and morphology [11,10], this is the first time that a thorough compositional study has been performed during the first stages of formation. If one matches the obtained information to the different types of morphology observed by Liu et al., one can assign the dense barrier layer to a lithium-exposed pseudoboehmite, while the columnar top layer can be assigned to an Al-Li layered double hydroxide.

4.2. Formation mechanism

Based on the results obtained with ToF-SIMS, the formation mechanism of the lithium-based protective layer proposed by Visser et al. [8] can be extended, as illustrated in Fig. 11 by different stages. Stage I is the phase where the scribe is first exposed to the neutral salt spray. The aqueous electrolyte induces leaching of lithium salts from the organic coating into the scribe. The leaching, on its turn, results in an increase of pH to alkaline conditions, and this in the presence of chlorides will trigger oxide thinning and induces the anodic dissolution of aluminium. Stage II describes the initial formation of the protective

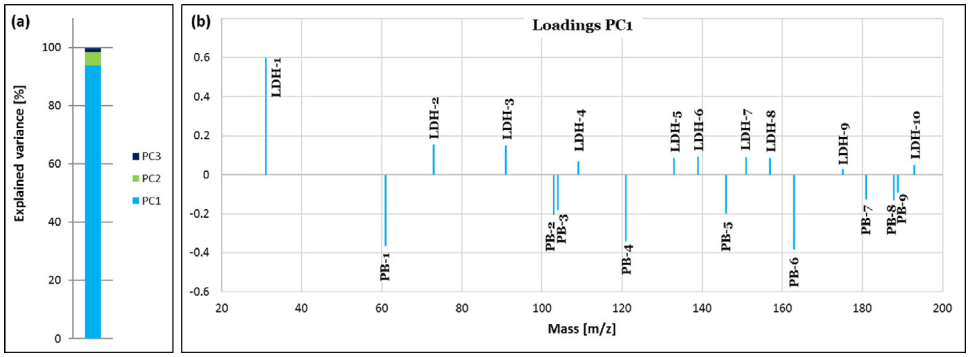

Fig. 6. (a) Distribution of the explained variance by principal components PC1–3. (b) Loadings for PC1. Peak assignments are provided in Table 2.

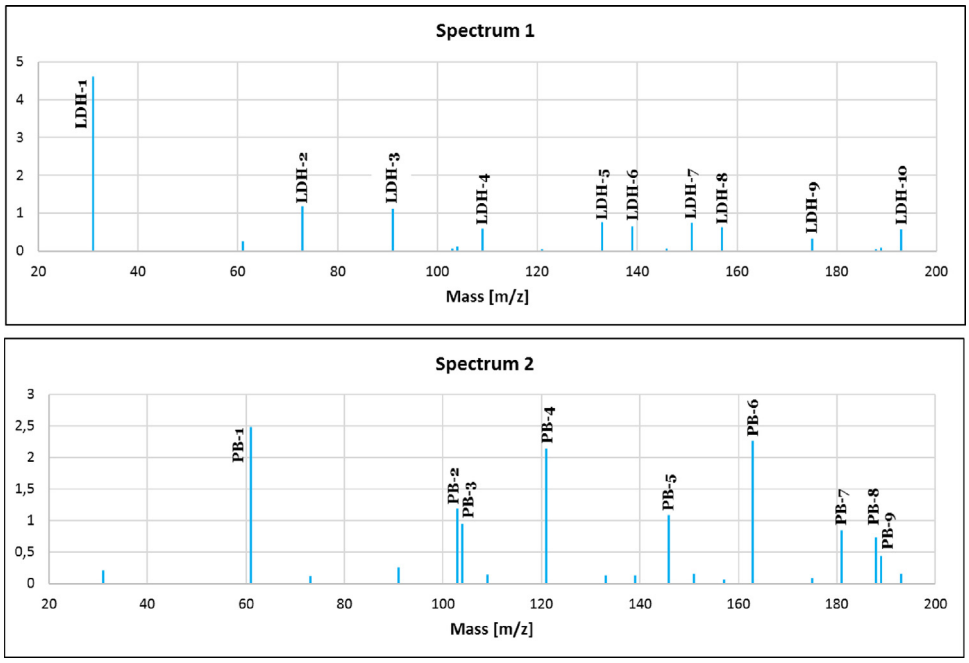

Fig. 7. Peaks comprising pure compounds obtained after 100 iterations of NMF. Top: compound 1. Bottom: compound 2.

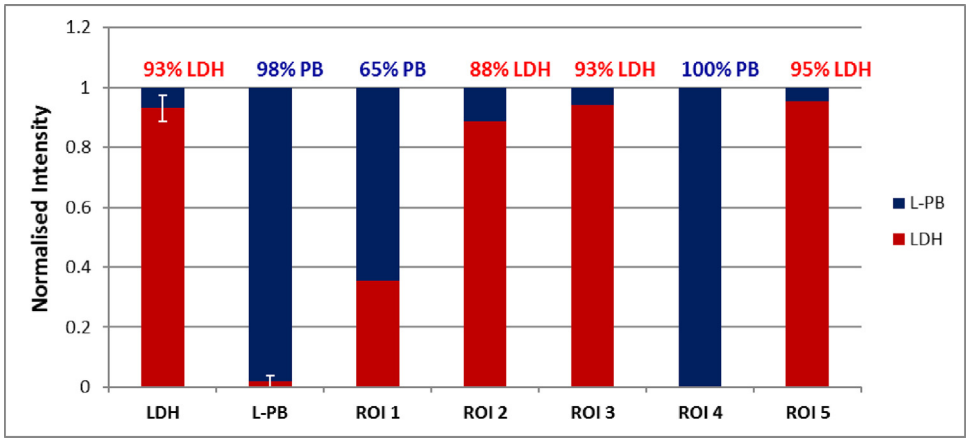

Fig. 8. Relative 'concentrations' for all samples of both the compounds obtained by NMF. The sum of components is normalised to 100%. Standard errors are shown in white for the LDH and L-PB references. ROIs 1–3 were selected in the 15 min NSS exposed scribe, ROIs 4–5 were selected in the 1 h NSS exposed scribe.

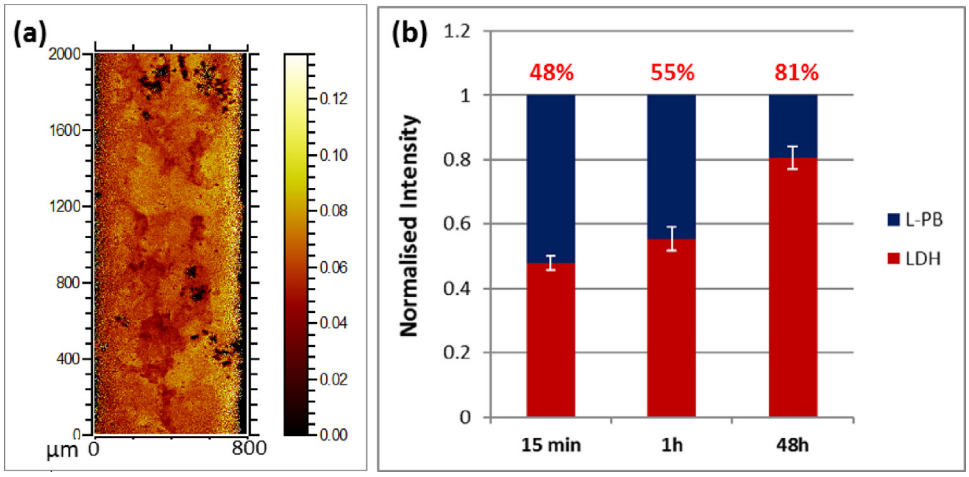

Fig. 9. (a) $^{6}Li^{+}$ image of an 48 h NSS exposed scribe. (b) NMF scores for the mass spectra obtained by large area (800 µm × 2000 µm) ToF-SIMS imaging of the 15 min, 1 h and 48 h NSS exposed scribes. Standard errors are shown in white.

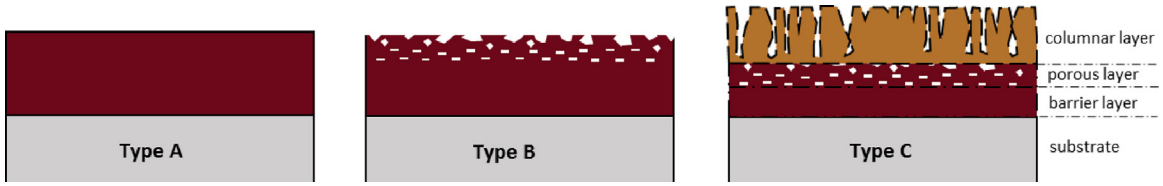

Fig. 10. Different types of morphology observed for the protective layer, based on [11].

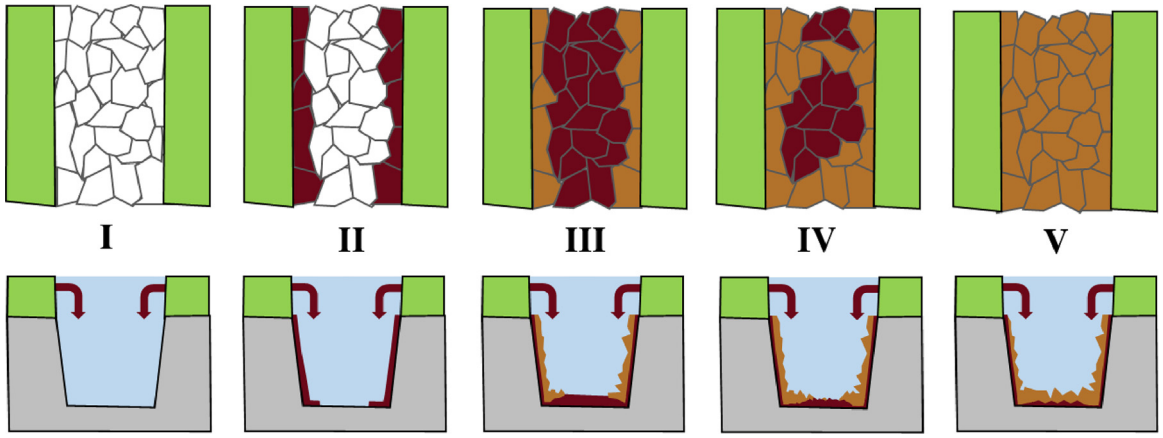

Fig. 11. Schematic presentation for the growth stages of the protective layer (based on [8]). Formation of a lithium-containing pseudoboehmite layer (red) is followed by the formation of a lithium-rich layered double hydroxide layer (orange) under exposure of a neutral salt spray. (For interpretation of the references to color in this legend, the reader is referred to the web version of the article.)

layer adjacent to the organic coating. Moderate alkaline conditions are reported, showing a local pH around 9–10 near the metal surface [8]. These alkaline conditions result in the formation of a hydrated aluminium oxide surface layer with a small amount of lithium incorporated in its matrix (L-PB). As lithium salts leach further into the scribe (stage III), the L-PB layer laterally grows towards the center of the scribe. This process goes relatively fast. In the meantime, the concentration of lithium salts exceeded a certain threshold near the organic coating, which initiates the formation of a columnar LDH layer. The conversion from a pseudoboehmite-type layer to an LDH is likely attributed to a local increase in pH in combination with a higher concentration of lithium, as it has been shown that Al-Li LDH conversion coatings can be prepared under strong alkaline conditions (pH 11–13) [4]. After longer exposure times to the neutral salt spray, the concentration of lithium species also increases in the center of the scribe, which enables growth of LDH in the center of the scribe as well (stage IV). Selective growth of the LDH layer is likely associated with different phases in the alloy or individual grains and with local cathodic and anodic activities [11]. In the anodic regions aluminium dissolves from the thick barrier layer. This explains why a porous layer has been found in the morphological investigations reported in literature (Fig. 10) [7,8,11]. A columnar LDH layer laterally grows at the surface, on the expense of the underlying L-PB barrier layer, until the scribe is completely covered with LDH (stage V).

5. Conclusions

Its high sensitivity towards lithium and its high lateral resolution makes that ToF-SIMS is ideally suited for the compositional investigation of a lithium-based corrosion protective layer formed in coating defects. For the first time, the leaching of lithium salts from a coating into a coating defect was successfully monitored as a function of NSS exposure time. The spread of lithium in 1-mm-wide scribes occurs relatively fast; after 15 min NSS exposure the scribes were already completely covered with lithium. A clear distinction between pseudoboehmite, lithium-containing pseudoboehmite and Al-Li layered double hydroxide layers could be made with ToF-SIMS. Investigation of the protective layer after varying NSS exposure time has led to the unravelling of its formation mechanism. Under exposure to a neutral salt spray, lithium salts leach in coating defects to induce growth of a lithium-containing pseudoboehmite barrier layer on the exposed AA2024-T3 substrate. After longer NSS exposure times, the lithium concentration in the defect increases, as well as the local pH. The barrier layer partially degrades by anodic dissolution of aluminium, while an Al-Li layered double hydroxide layer starts to grow and eventually covers the surface.

Author contributions

P.V. prepared the samples and supported the research; K.M. performed the experiments; K.M. analyzed the data; G.F.T., M-L.A. and J.F.W. provided the simsMVA app and supported the ToF-SIMS and MVA analysis; K.M. wrote the paper; J.M.C.M., H.T. and T.H. supervised the research. All authors were involved in the editing of the manuscript.

Conflicts of interest

The authors declare no conflict of interest.

Acknowledgements

T.H. acknowledges financial support by Research Foundation – Flanders (FWO).

Appendix A

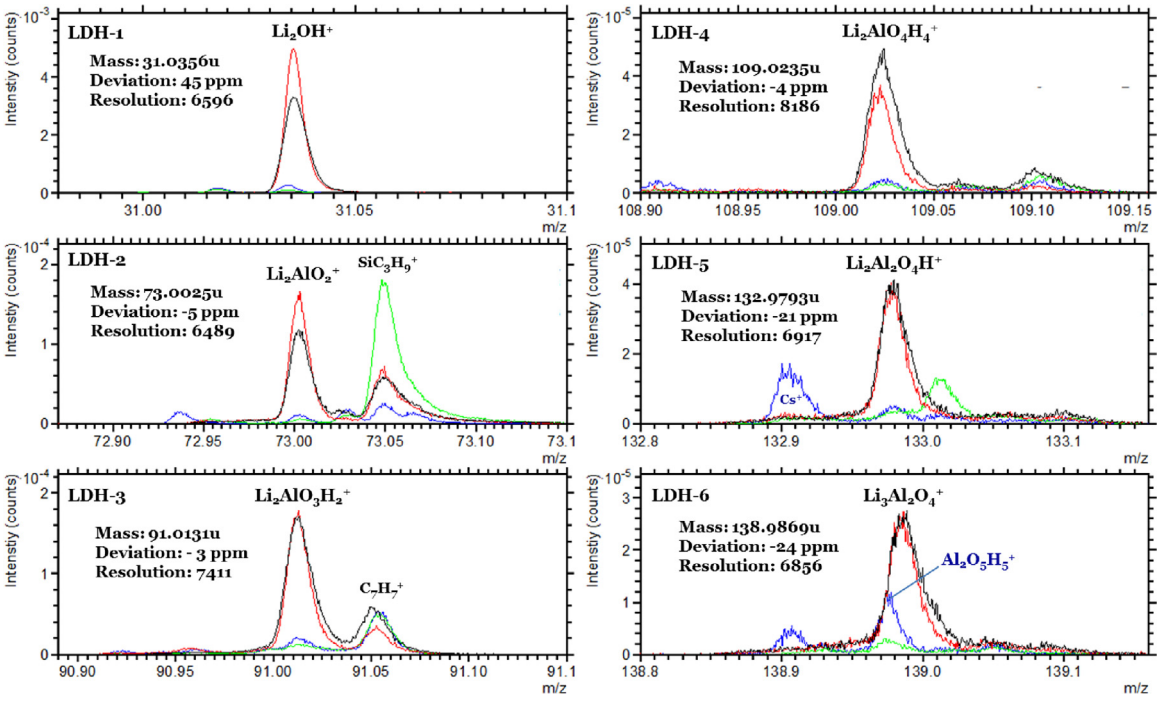

Fig. A.1. Detailed mass spectra of peaks LDH-1-6. Overlay of reference sample L-PB in blue, reference sample LDH in red, ROI 4 in green and ROI 5 in black. (For interpretation of the references to color in this legend, the reader is referred to the web version of the article.)

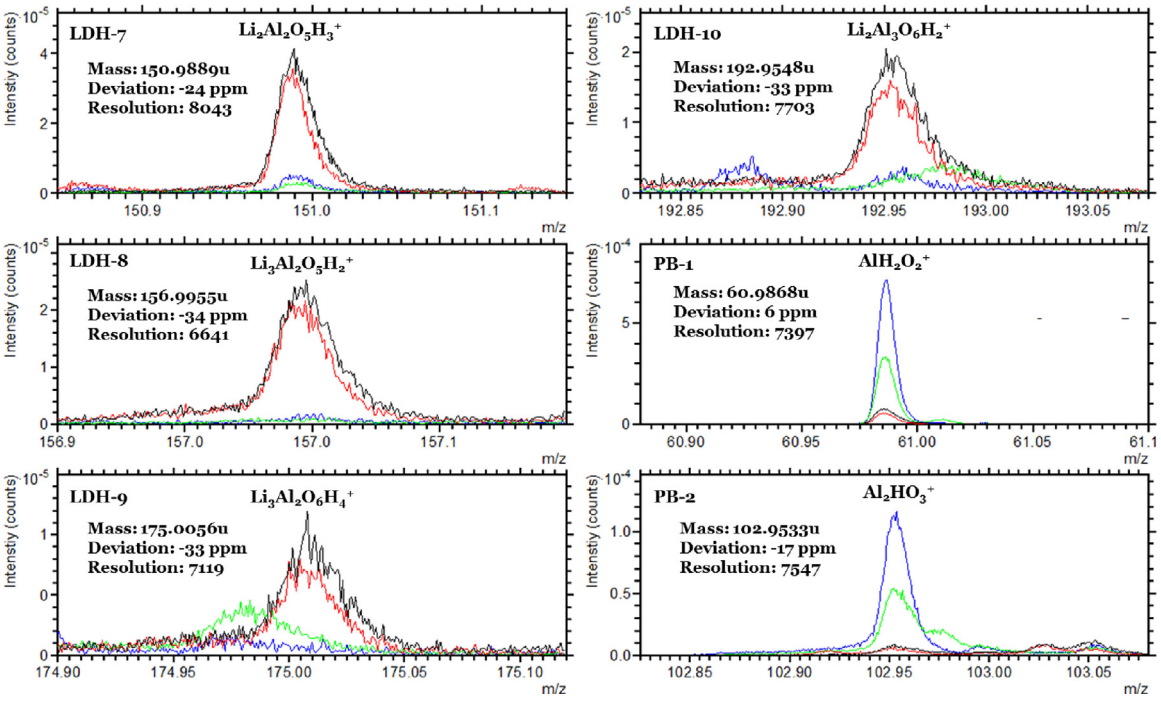

Fig. A.2. Detailed mass spectra of peaks LDH-7-10 and PB-1-2. Overlay of reference sample L-PB in blue, reference sample LDH in red, ROI 4 in green and ROI 5 in black. (For interpretation of the references to color in this legend, the reader is referred to the web version of the article.)

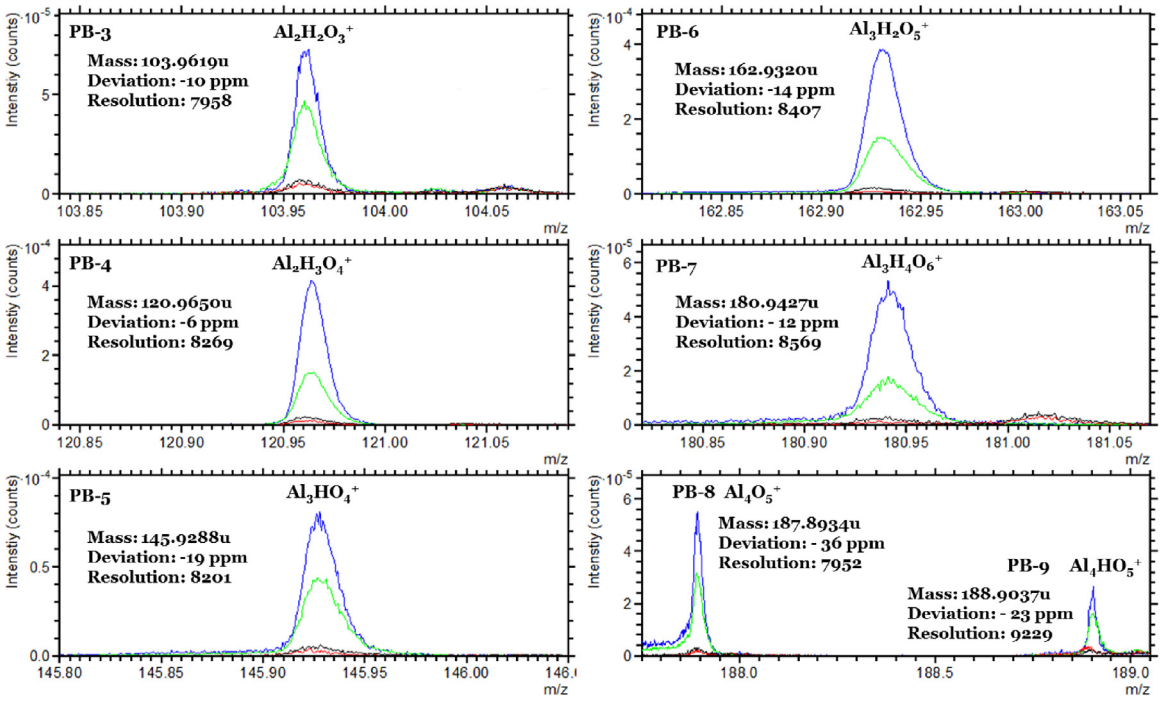

Fig. A.3. Detailed mass spectra of peaks PB-3-9. Overlay of reference sample L-PB in blue, reference sample LDH in red, ROI 4 in green and ROI 5 in black. (For interpretation of the references to color in this legend, the reader is referred to the web version of the article.)

References

[1] A.E. Hughes, I.S. Cole, T.H. Muster, R.J. Varley, Designing green, self-healing coatings for metal protection, NPG Asia Mater. 2 (4) (2010) 143–151.

[2] J. Gui, T.M. Devine, Influence of lithium on the corrosion of aluminum, Scr. Metall. 21 (6) (1987) 853–857.

[3] C.M. Rangel, M.A. Travassos, The passivation of aluminium in lithium carbonate/bicarbonate solutions, Corros. Sci. 33 (3) (1992) 327–343.

[4] R.G. Buchheit, M.D. Bode, G.E. Stoner, Corrosion-resistant, chromate-free talc coatings for aluminum, Corros. Sci. 50 (3) (1994) 205–214.

[5] C.A. Drewien, M.O. Eatough, D.R. Tallant, C.R. Hills, R.G. Buchheit, Lithium-aluminium-carbonate-hydroxate hydrate coatings on aluminum alloys: composition, structure, and processing bath chemistry, J. Mater. Res. 11 (1996) 1507–1513.

[6] P. Visser, H. Terryn, J.M.C. Mol, Aerospace coatings: active protective coatings, in: A. Hughes, J. Mol, M. Zheludkevich, R. Buchheit (Eds.), Active Protective Coatings – New-Generation Coatings for Metals, 233rd ed., Springer, The Netherlands, 2016, pp. 315–372 (Chapter 12).

[7] P. Visser, Y. Liu, X. Zhou, T. Hashimoto, G.E. Thompson, S.B. Lyon, L.G.J. van der Ven, A.J.M.C. Mol, H.A. Terryn, The corrosion protection of AA2024-T3 aluminium alloy by leaching of lithium-containing salts from organic coatings, Faraday Discuss. 180 (2015) 1–16.

[8] P. Visser, A. Lutz, J.M.C. Mol, H. Terryn, Study of the formation of a protective layer in a defect from lithium-leaching organic coatings, Prog. Org. Coat. 99 (2016) 80–90.

[9] P. Visser, Y. Liu, H. Terryn, J.M.C. Mol, Lithium salts as leachable corrosion inhibitors and potential replacement for hexavalent chromium in organic coatings for the protection of aluminum alloys, J. Coat. Technol. Res. 13 (4) (2016) 557–566.

[10] Y. Liu, P. Visser, X. Zhou, S.B. Lyon, T. Hashimoto, A. Gholinia, G.E. Thompson, G. Smyth, S.R. Gibbon, D. Graham, J.M.C. Mol, H. Terryn, An investigation of the corrosion inhibitive layers generated from lithium oxalate-containing organic coating on AA2024-T3 aluminium alloy, Surf. Interface Anal. 48 (8) (2016) 798–803.

[11] Y. Liu, P. Visser, X. Zhou, S.B. Lyon, T. Hashimoto, M. Curioni, A. Gholinia, G.E. Thompson, G. Smyth, S.R. Gibbon, D. Graham, J.M.C. Mol, H. Terryn, Protective film formation on AA2024-T3 aluminum alloy by leaching of lithium carbonate from an organic coating, J. Electrochem. Soc. 163 (3) (2016) C45–C53.

[12] P. Visser, M. Meeusen, Y. Gonzalez-Garcia, H. Terryn, J.M.C. Mol, Electrochemical evaluation of corrosion inhibiting layers formed in a defect from lithium-leaching organic coatings, J. Electrochem. Soc. 164 (7) (2017) 396–406.

[13] L. Van Vaek, Molecular speciation analysis of inorganic compounds, in: J. Vickerman, D. Briggs (Eds.), ToF-SIMS: Materials Analysis by Mass Spectrometry, 2nd ed., IM Publications and Surface Spectra Limited, 2013, pp. 125–149 (Chapter 15).

[14] E. Stumpe, A. Benninghoven, Surface oxidation studies of iron using the static method of secondary ion mass spectrometry (SIMS), Phys. Status Solidi (A) 21 (2) (1974) 479–486.

[15] J.D. Gorman, A.E. Hughes, D. Jamieson, P.K.J. Paterson, Oxide formation on aluminum alloys in boiling deionised water and NaCl, $CeCl_3$ and $CrCl_3$ solutions, Corros. Sci. 45 (6) (2003) 1103–1124.

[16] J. Shlens, A Tutorial on Principal Component Analysis, 2014, April 7; Version 3.02, Retrieved from arXiv Database, arXiv:1404.1100, 2014.

[17] J.L.S. Lee, B.J. Tyler, M.S. Wagner, I.S. Gilmore, M.P. Seah, The development of standards and guides for multivariate analysis in surface chemical analysis, Surf. Interface Anal. 41 (2) (2009) 76–78.

[18] G.F. Trindade, M.L. Abel, J.F. Watts, Non-negative matrix factorisation of large mass spectrometry datasets, Chemom. Intell. Lab. Syst. 163 (November) (2017) 76–85.

[19] D.D. Lee, H.S. Seung, Learning the parts of objects by non-negative matrix factorization, Nature 401 (6755) (1999) 788–791.

[20] G. F. Trindade, M. L. Abel, J. F. Watts, simsMVA, Available at: www.mvatools.com, 2017.

[21] G.F. Trindade, J. Bañuls-Ciscar, C.K. Ezeh, M.L. Abel, J.F. Watts, Characterisation of wood growth regions by multivariate analysis of ToF-SIMS data, Surf. Interface Anal. 48 (7) (2016) 584–588.